JOURNAL OF SOLID STATE CHEMISTRY 33, 63–82 (1980).

An Electron Microscopy Study of Crystallography and Phase Relationships in the Be_3N_2–$BeSiN_2$ System

T. M. SHAW AND G. THOMAS

Department of Materials Science and Mineral Engineering, University of California, Berkeley, and Materials and Molecular Research Division, Lawrence Berkeley Laboratory, Berkeley, California 94720

Received February 1, 1979; in revised form July 27, 1979

Transmission electron microscopy and diffraction have been used to examine structural aspects of phases along the $BeSiN_2$–Be_3N_2 tie line of the Be–Si–O–N system. Electron diffraction experiments are found to substantiate previous X-ray evidence for the derived structures of $BeSiN_2$, β-Be_3N_2, and α-Be_3N_2 and the presence of a number of long-period superstructures at intermediate compositions. Real space observations using direct fringe and structure imaging techniques have been made and are in agreement with the 15*R* polytype structure derived from X-ray diffraction data. This structure is composed of coherent intergrowths of $BeSiN_2$ and β-Be_3N_2. Further observations made on a nonstoichiometric $BeSiN_2$ sample suggest that the polytypes may be described in terms of a regularly faulted $BeSiN_2$ structure. Each fault changes the coordination of tetrahedral sites from base sharing to edge sharing in the fault, allowing excess beryllium atoms to be accommodated in the close-packed nitrogen lattice. For larger deviations from the $BeSiN_2$ stoichiometric composition, a higher density of faults occur which interact to form ordered arrangements and the observed polytype structures. The present observations establish that polytypism in the Be–Si–N system is related to the general phenomenon of crystallographic shear as observed in other complex oxide and ceramic systems. It is suggested that similar faulting may account for the polytype structures in other sialon systems.

I. Introduction

Since the discovery of the β' phase in the Si–Al–O–N system simultaneously by Jack and Wilson in Great Britain (*1*), and Oyama and Kamigaito (*2*) and Tsuge *et al.* (*3*) in Japan, the existence of a large number of nitrogen ceramic phases has been demonstrated (*4–7*). This discovery has opened up a new field of ceramic technology in which the potential for extensive alloying of ceramics has been identified. Composition control in sialon ceramics shows promise as a means by which properties such as strength, creep resistance, and oxidation resistance may be optimized (*8–10*). Alloying to produce materials which are easier to fabricate and the possibility of pressureless sintering to theoretical density in sialon ceramics are also being investigated (*11*).

Characterization of the crystal structures of a number of phases has been carried out using X-ray analysis in the Si–Al–O–N, metal sialon (*4*), Be–Si–O–N (*5, 6*), and silicon lanthanide oxynitride (*12*) systems and electron diffraction in the Si–Al–O–N system (*13*). Nevertheless, a large number of systems have yet to be analyzed.

One such group of phases is a related series of structures first reported by Jack (*4*) at AlN-rich compositions in the Si–Al–O–N system. Each phase extends along a line of constant metal to nonmetal atom ratio ($M:X$) and has a narrow range of

0022-4596/80/070063-20$02.00/0

homogeneity. Similar series have since been reported in the Be–Si–O–N (*5*), Mg–Si–Al–O–N, and Li–Si–Al–O–N systems. Structural determinations using X-ray powder diffraction techniques have identified these phases as wurtzite polytypes (*4*, *5*), in which the unit-cell dimensions are determined by composition rather than by the periodicity of displacement faulting. In the Be–Si–O–N system for metal to nonmetal atom ratios of $M_{m+1}:X_m$, a series of eight polytypes has been reported between Be_3N_2, $BeSiN_2$, and BeO (Fig. 1). The index m assumes a minimum value of 2 for β-Be_3N_2 and a maximum value of $m=\infty$ corresponding to both the wurtzite structure BeO and the ordered wurtzite structure $BeSiN_2$. The composition dependence of the series can be explained by regular insertion of a cubic close-packed layer in which all tetrahedral sites are occupied by metal atoms (composition M_2X) into the hexagonal wurtzite layer arrangement (*5*). In the wurtzite structure tetrahedral sites share bases, thus only upward or downward pointing sites may be occupied, to give the composition MX. The period of the M_2X layers then determines the overall composition and the unit-cell dimensions of each polytype. For example, in the $15R$ $Be_9Si_3N_{10}$ ($M_6:X_5$) structure an M_2X layer occurs every fifth layer to produce a unit cell consisting of three rhombohedrally related blocks each containing five close-packed layers. In the same way other members of the series can be produced, i.e., $9R$, $8H$, $12H$, $21R$, and $27R$ after the notation of Ramsdell (*14*).

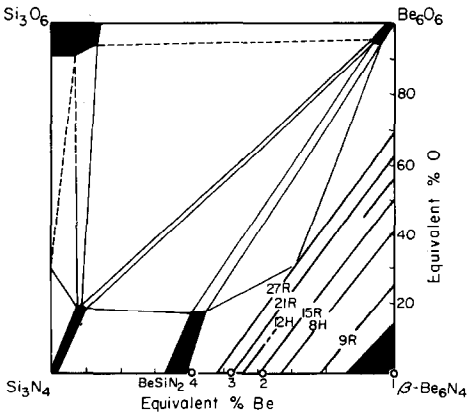

FIG. 1. An isothermal section through the Be–Si–O–N phase diagram at 1780°C after Thompson and Gauckler (*33*).

The object of this investigation was to examine in detail the crystallography of polytypes in the series Be_3N_2–$BeSiN_2$ using high-resolution transmission electron microscopy and diffraction techniques. Phase contrast was used to examine stacking periodicities of the close-packed planes and so to characterize disorders occurring in the stacking sequence. Defects in the polytype structures were also examined using contrast experiments and their role in polytype formation was examined. Alternative descriptions of the polytype phases in terms of polysynthetic twinning and crystallographic shear were investigated. Where possible, the results have been extended to the description of similar series in the Be_3N_2–BeO and other systems.

II. Experimental Procedures

II.1. Materials Preparation

The materials for this study were prepared at the Max Planck Institute in Germany and are listed as follows. Details of their preparation are given by Huseby *et al.* (*6*).

Sample (1) Beryllium nitride
Composition: β-Be_3N_2
Structure: $Be_3N_2(4H)$
(99%)

Sample (2) Beryllium silicon nitride
Composition: $Be_9Si_3N_{10}$
Structure: $15R$ + trace $8H$

Sample (3) Beryllium silicon nitride
Composition: $Be_{11}Si_5N_{14}$
Structure: $21R$ + trace $12H$

Sample (4) Beryllium silicon nitride
Composition: 60% $BeSiN_2$ + 40% $Be_{6.5}Si_{3.5}N_9$
Structure: $BeSiN_2$ + $27R$

All these specimens have compositions lying along the Be_3N_2–$BeSiN_2$ tie line of the Be–Si–O–N phase diagram (Fig. 1).

II.2. Transmission Electron Microscopy

Slices 0.02 mm thick were cut from the bulk materials using a diamond sectioning wheel. These were then ground by hand to a thickness of about 0.004 mm using silicon carbide papers. Ion beam milling was used to thin 2.3-mm disks cut from each slice to electron transparency. In order to prevent charging of the specimen under the influence of the electron beam and improve image stability in the microscope, a thin (10–30 Å thick) layer of carbon was evaporated on one side of the specimen.

Each material was examined by selected area diffraction, conventional imaging, and high-resolution imaging techniques using the Siemens 102 and Philips 301 microscopes operating at 125 and 100 kV, respectively. The Siemens 102 was equipped with a high-angle tilt stage for precise orientation of the specimen and contrast experiments. High-voltage electron microscopy was also employed (Hitachi, 650 kV) for examination of thicker areas of the samples and accurate selected area diffraction.

III. Experimental Results

III.1. Structure of Be_3N_2

Selected area diffraction patterns from single grains of sample 1 tilted to high-symmetry orientations were recorded in order to determine the extent of occurrence of the α and β modifications of Be_3N_2 and to compare them to the structures found by X-ray diffraction (*15–17*). All observed diffraction patterns were indexed and could be accounted for by one of the two modifications confirming the X-ray determined structures. Equiaxed grains 5–10 μm in diameter of both α and β structures were observed, a higher proportion being of the β form. From X-ray diffraction analysis sample 1 was determined to consist of 99% β-Be_3N_2. The high proportion of grains of the α form found indicates that more material remained untransformed to β during hot pressing than was found by X rays (*6*).

III.2. Structure of $BeSiN_2$

The structure of $BeSiN_2$ has been previously determined by X-ray analysis of single crystals to be a partially ordered wurtzite structure (*18*). Ordering of the metal atoms, Be and Si, reduces the hexagonal symmetry of the wurtzite arrangement to orthorhombic symmetry with $a_0 = 4.977$ Å, $b_0 = 5.747$ Å, and $c_0 = 4.674$ Å. Three variants of the ordered structure related by a rotation of 120° about the [001] direction have been found to occur in single crystals. Examination of sample 4 showed that grains consisted predominantly of a wurtzite structure but contained large numbers of planar defects which will be discussed later.

Electron diffraction from individual regions of perfect crystal produced sharp fundamental reflections corresponding to the wurtzite structure. Superlattice reflections resulting from the ordered structure were observed and varied from diffuse intensity to sharp, well-defined spots in selected area diffraction patterns (Figs. 2c and d). A typical region is shown in Fig. 2a for a foil zone axis near [001]. A dark field image was taken using the two reflections indicated by the arrows and appears in Fig. 2b. This shows that part of the region contained well-ordered domains about 400–600 Å across.

Stereoscopic analysis and application of the so-called $2\frac{1}{2}$D technique (*19*) showed that reflections marked 1 and 2 (Fig. 2c) arise from two ordered variants of the $BeSiN_2$ structure. The third variant contributes to reflection 3 of Fig. 2c. The speckled contrast in the image (Fig. 2b) is associated with the diffuse reflections shown in Fig. 2d and could be due to short-range order (or small ordered domains).

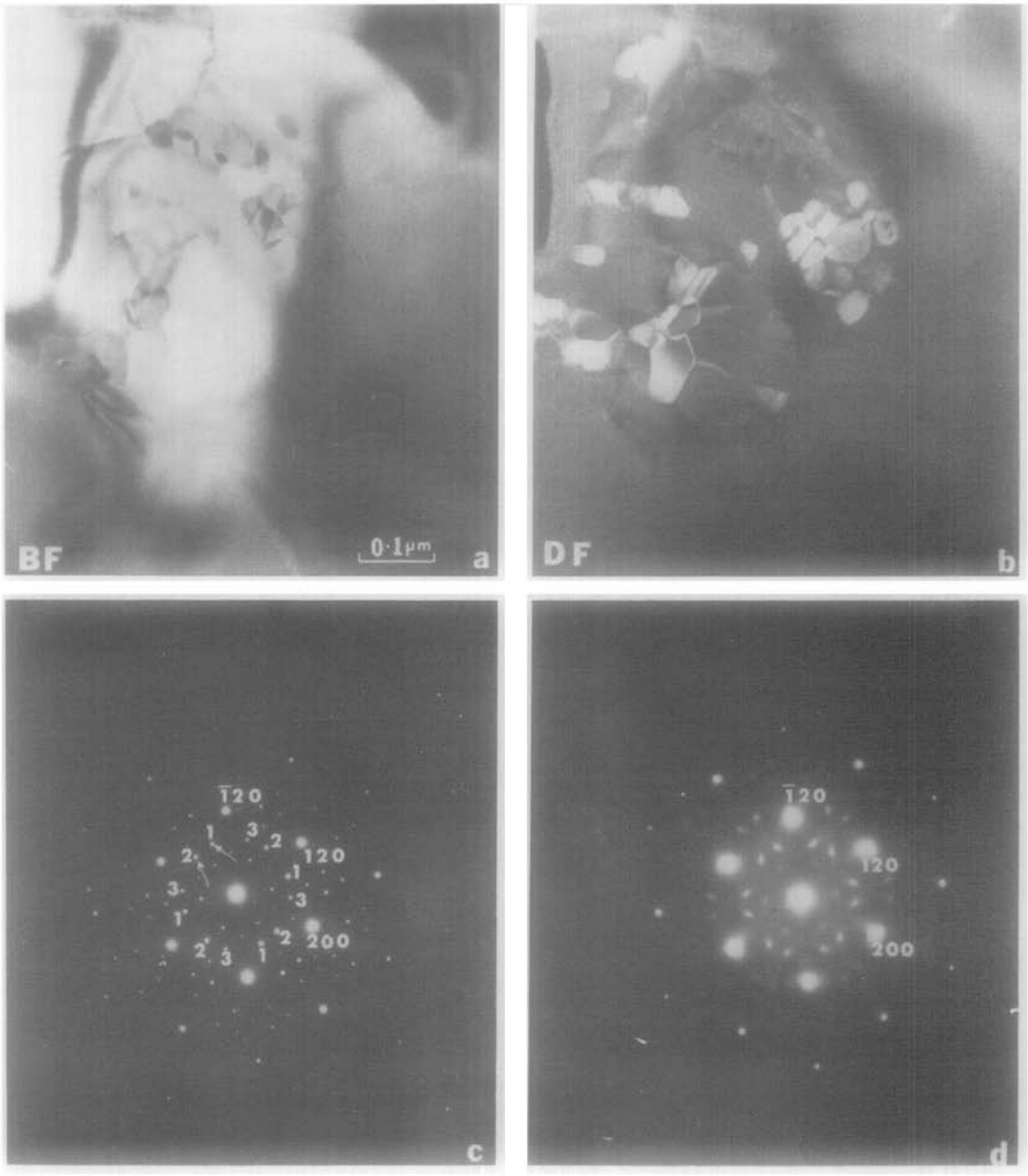

FIG. 2. Ordered domains of $BeSiN_2$ structure, (001) orientation. (a) Bright field, (b) dark field taken using two superlattice reflections indicated by arrows in (c). In (d) diffuse superlattice reflections are observed in the SAD taken from an adjacent region.

These observations are in agreement with the X-ray determined structure of $BeSiN_2$. The occurrence of well-ordered regions suggests that the structure may, however, be fully ordered in some regions.

III.3. Structure of 15R $Be_9Si_3N_{10}$ Polytype

High-resolution phase contrast imaging was used to examine the structure of sample 2, reported to consist predominantly of the

15*R* polytype structure. Electron diffraction patterns obtained from single grains indicated that while extensive regions of well-ordered polytype structure were found, in addition, there were regions of mixed or disordered polytype structures. The latter will be discussed in more detail in the following.

Both one- and two-dimensional lattice fringe images were recorded from well-ordered regions of the 15*R* structure. Details of these results are presented elsewhere (*20, 21*), but the essential findings are illustrated in Fig. 3 in which a two-dimensional fringe image of the 15*R* structure is compared with the projected X-ray structure (*4, 5*). The image is seen to consist of identical blocks of contrast as outlined. Each block consists of five closed-packed layers, adjacent blocks being related by a translation of $\frac{1}{3}\langle 110\rangle$. This gives rise to an overall repeat stacking of 15 close-packed layers with rhombohedral symmetry. Two out of the five fringes in each block have lighter contrast than the rest. This indicates that two out of the five close-packed layers in each block have a different stacking arrangement compared to the remaining three. Examination of combinations of hexagonal and cubic stacking of the close-packed layers showed that a single stacking sequence is consistent with these observations, i.e., that found by X-ray diffraction. This structure is shown in projection in Fig. 3 for comparison. The structure can be considered to consist of a mixture of three layers of $BeSiN_2$ and two layers of β-Be_6N_4 as expected from the 15*R* composition ($Be_9Si_3N_{10}$) along the tie line $BeSiN_2$–Be_3N_2 (point 2, Fig. 1) (*21*).

III.4. Twinning and Disorders in the Polytype Structure

The contrast behavior of a region of 15*R* structure was examined by tilting (Fig. 4). With the electron beam parallel to the [010] direction, contrast was uniform throughout the grain in a bright field imaging mode (Fig. 4a). When the grain was tilted about the

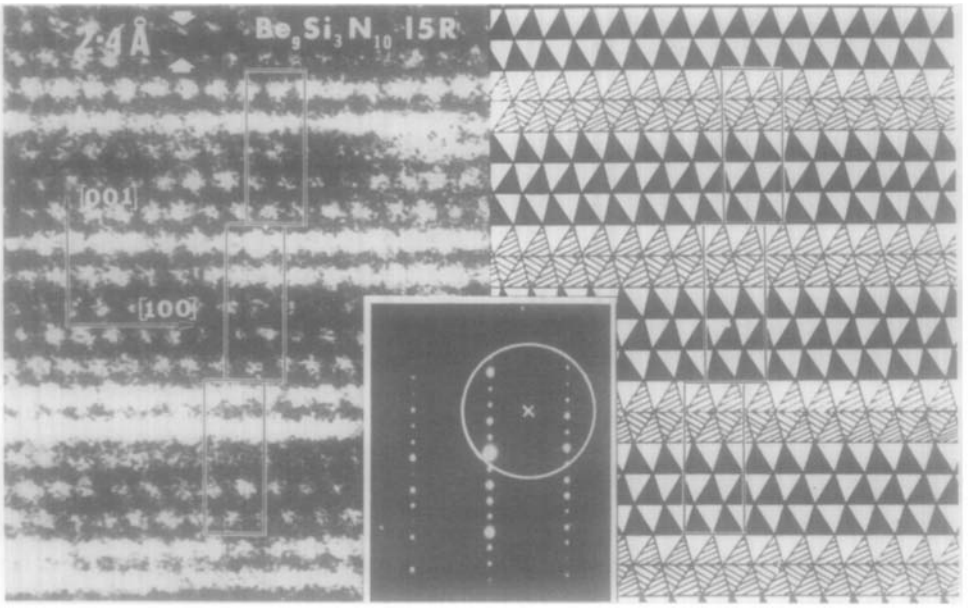

FIG. 3. Comparison of a high-resolution image of the 15*R* structure with the projection of the structure found by X-ray diffraction. Marked are the outlines of the three identical structural blocks which make up the unit cell. Inset is the diffraction geometry used for imaging; X marks the position of the optic axis.

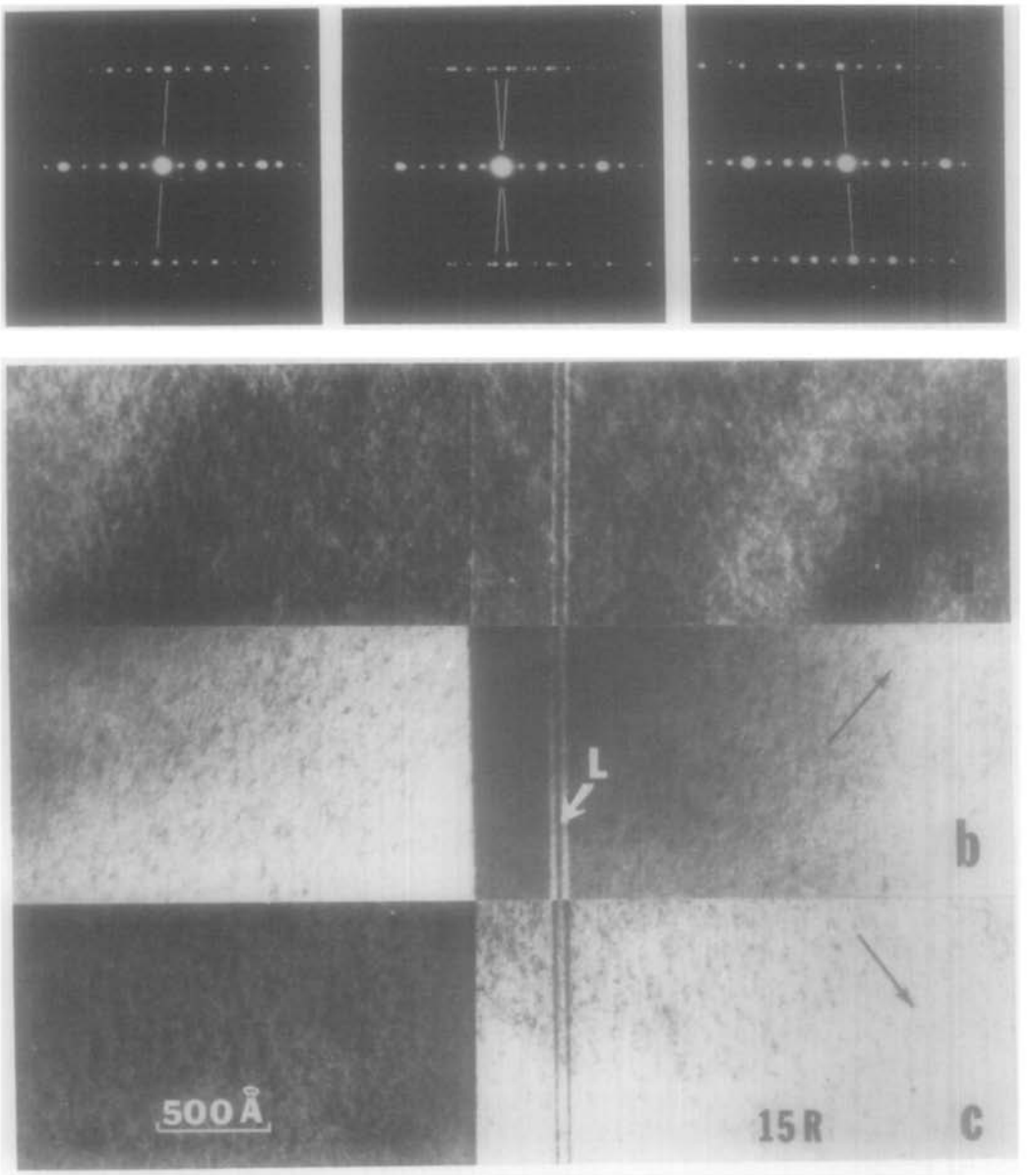

FIG. 4. The effect of tilting on contrast across a twin boundary in a disordered 15*R* polytype structure. (a) Bright field in a symmetrical (010) orientation, (b and c) bright field images of the boundary, when tilted a small amount about the directions indicated by the arrows. Differential contrast is seen between the twins. SAD from either side and across the boundary confirms the twin relation.

directions indicated by the arrows (Figs. 4b and c) alternate dark and light bands appeared, with the contrast being reversed (Fig. 4c). This contrast behavior arises from twins (*22*), as confirmed by selected area diffraction patterns. The twin boundary is the close-packed plane. In addition to the main twin, two thin twin lamellae (L in Fig. 4) occur close to the boundary.

In Fig. 5 the tilted image of a region containing a large number of such twins is compared with a high-resolution image of

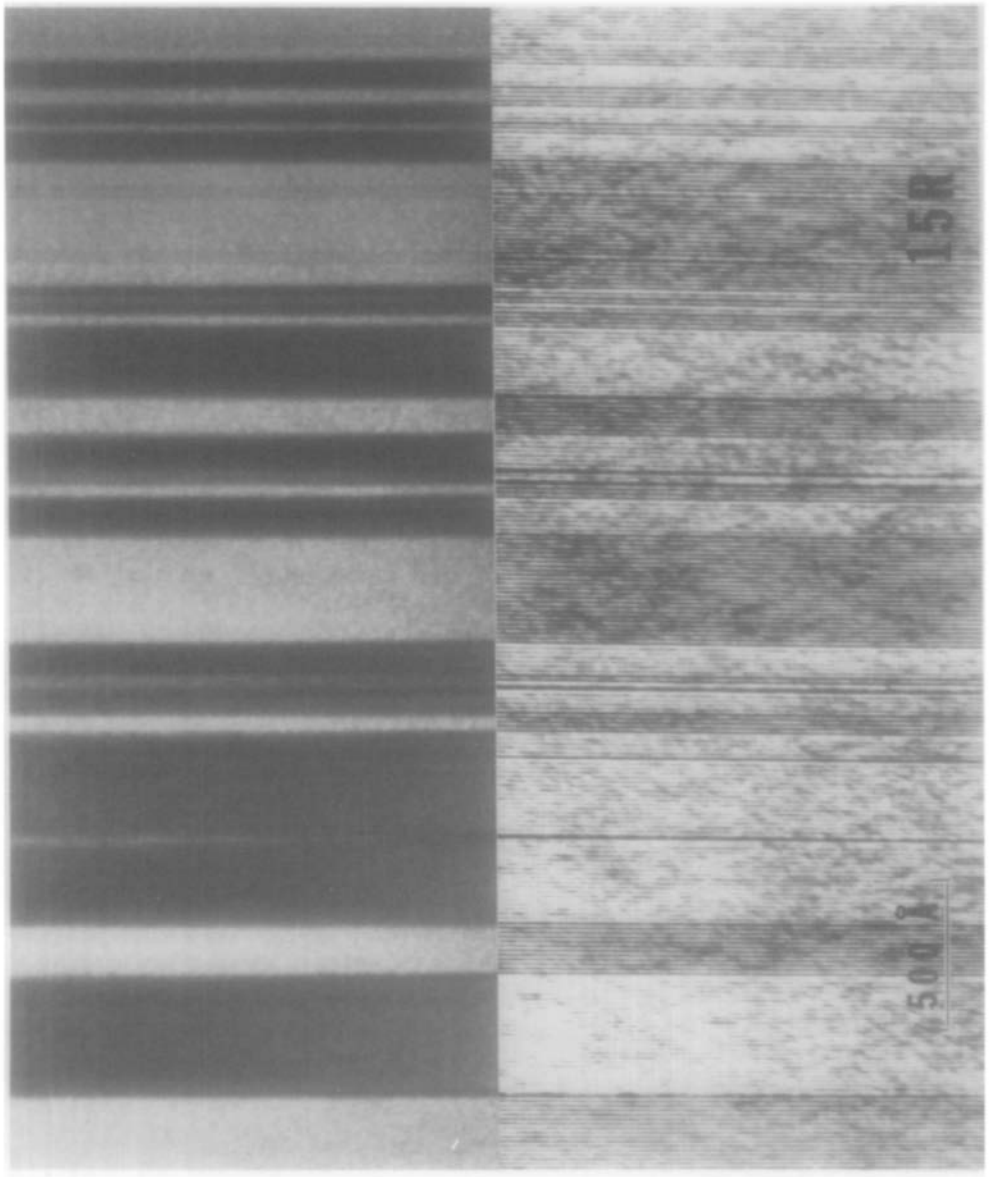

FIG. 5. Comparison of a high-resolution image of block spacings in a polytype structure with the image of twin bands in the same region made visible by tilting. Associated with each twin boundary is a disordered block spacing.

the block spacings in the same area. Associated with each twin interface is disorder in the regular $15R$ block spacing. The way in which a twin of this kind arises structurally can easily be visualized.

The $15R$ structure can be considered as being made up of identical blocks of five close-packed layers. Each block is related to the adjacent block by a displacement of $\frac{1}{3}[100]$ as in Fig. 3. This produces a layer of cubic stacking between the blocks. In the twin the displacement relating blocks is in the opposite direction, i.e., $-\frac{1}{3}[100]$. This is equivalent to a 180° rotation of the structure about the [001] direction. A perfect $15R$ structure is then represented using the stacking symbols A, B, and C as

$$A^m_m C^m A^m C^m A^m C^m_m B_m C_m B_m C_m B^m_m A^m \cdot B^m A^m B^m A^m_m C,$$

after the notation of Thompson (*5*).

Changing the stacking sequence of the blocks so that a twin results, the stacking sequence across the twin plane becomes

matrix | twin

$$A^m_m C^m A^m C^m A^m C^m_m B_m C_m B_m C_m B^m_m A^m B^m \; A^m \; B^m A^m B^m_m C_m B_m C_m B_m C^m_m A^m C^m A^m C^m A^m E$$

twin plane

The change in stacking produces an extra layer of hexagonal stacking followed by a cubic M_2X layer. This is equivalent to the insertion of one block of six close-packed layers instead of five or one extra hexagonal close-packed layer.

In this way twins can arise in all the rhombohedral polytypes by the inclusion of a block consisting of an even number of close-packed planes. In the hexagonal polytypes each block is the twin of the adjacent block as they consist of an even number of close-packed planes. Insertion or removal of one hexagonally close-packed layer locally removes this twin relationship over a region of crystal two blocks wide. Each change in block size results in a local change in composition due to the change in the periodicity of the M_2X cubic-stacked layers in the structure. It is clear from this model that local variations in composition, disordering of the structure, and the resulting twins are inseparable. Also, the twins are of the type described by Andersson and Hyde, i.e., chemical twins rather than mechanical twins (*23*).

Inclusion of more blocks of the next member of the series into the $15R$ structure results in more frequent twinning of the structure. The composition of the structure approaches that of the next member of the series. Finally, twinning of every block occurs and the next member of the series results, having a hexagonal structure. An example of this kind of intergrowth was observed by imaging the block spacings across a single grain as shown in Fig. 6. A regular spacing of 12.1 Å occurs in the top left-hand corner, indicating a region of well-ordered $15R$ structure. However, on crossing the grain the structure becomes disordered.

The selected area diffraction pattern taken using a 1-μm aperture centered on the disordered region contained reflections corresponding to both the $15R$ and $8H$ structures. By taking laser optical diffraction patterns from regions of the image 100 Å across using a small aperture, it was possible to discern regions of well-ordered $15R$ and $8H$ block periodicity within the disordered region. Further across the grain, a region of well-ordered $8H$ structure occurs (bottom right of Fig. 6), as indicated by the occurrence of a regular block fringe spacing of 9.6 Å. The transition from well-ordered $15R$ structure to well-ordered $8H$ structure occurs over a distance of about 0.5 μm. The

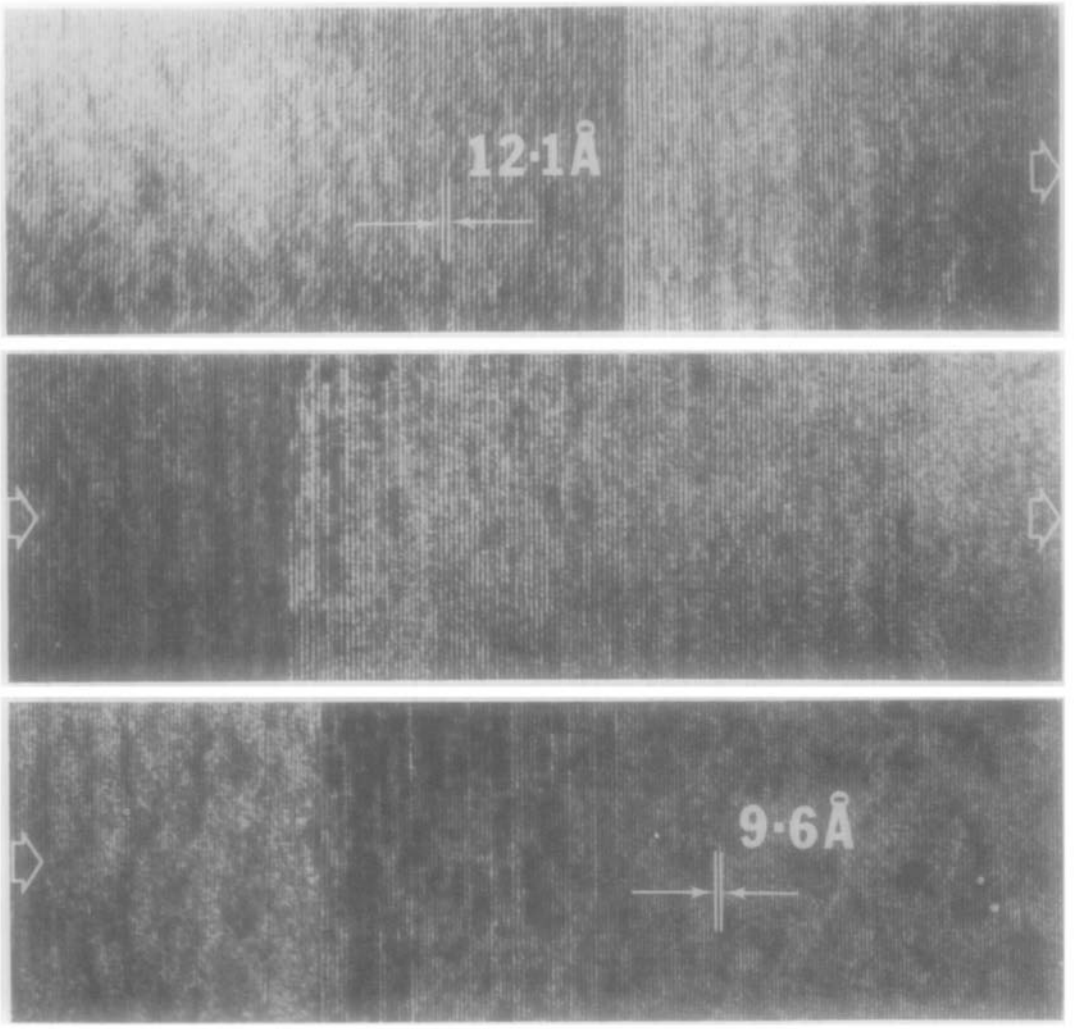

FIG. 6. Direct resolution of the block spacings across a single grain of polytype structure showing an intergrowth between a well-ordered 15*R* structure (top left) and a well-ordered 8*H* structure (bottom left) via a disordered region.

corresponding composition change is then $Be_9Si_3N_{10}$ to $Be_5Si_2N_6$. The transition occurs via a region of mixed 15*R* and 8*H* structural blocks. It seems likely that the transitions from one member of the polytype series to the next occur in the same manner when local fluctuations in composition arise within a grain. Grains with a uniform composition throughout will then consist of a proportional mixture of blocks of two adjacent polytype structures. Grains of completely ordered structure will only occur at the exact polytype compositions.

III.5. Twin Terminations

A number of twins made visible by tilting were seen to terminate within grains at an incoherent interface. Imaging the block spacing in a [100] foil orientation was done so as to examine the terminations (Fig. 7). The change in block spacing (A) produces a twin; the second change in block spacing

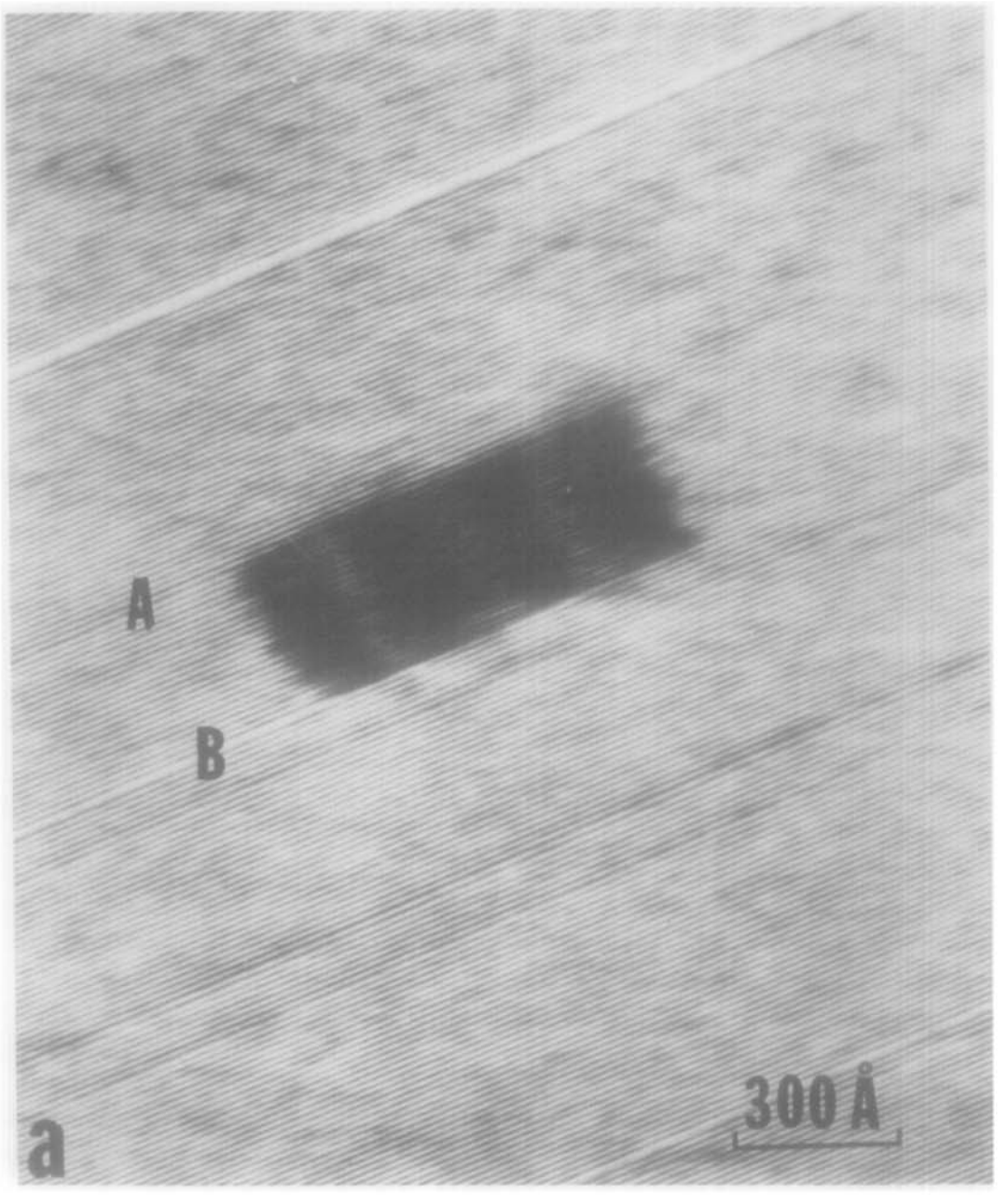

FIG. 7. High-resolution image of a twin termination in the 15*R* structure.

removes the twin relation (B). The disorders terminate at the region in dark contrast, indicating the termination of the twin. Inclination of the interface is indicated by broad depth fringes in the boundary image. Contrast analysis (not presented here) indicated that the dislocations terminating the twins were simple partials with their Burgers vectors in the close-packed planes. Glissile motion of the twin terminations is

therefore possible thus providing a mechanism by which changes in the spacing of M_2X layers can occur.

III.6. Faults in the $BeSiN_2$

Examination of grains in sample 4 showed that many grains consisting predominantly of $BeSiN_2$ contained a high density of structural irregularities. Two types of planar defect were observed. The first consisted of defects which lay in the close-packed planes exhibiting contrast characteristic of stacking faults or thin precipitates. The faults resulted in a continuous streak in the [001] direction in reciprocal space, indicating the faults were one or two close-packed layers thick. A second kind of defect was observed to lie on curved surfaces in the foil, at an angle to the close-packed plane. These again gave rise to fringe-type contrast for several diffracting conditions. The results of Section III.2 showed that the ordering of the Be and Si atoms is incomplete or consists of small domains of all three ordered variants. Macroscopically the crystal structure of $BeSiN_2$ grains can, therefore, be considered as being disordered possessing the full hexagonal symmetry of a wurtzite structure. Drum (*24*) considered the contrast arising from such faults in a wurtzite structure.

Reasonable displacement vectors for faults in the close-packed planes would be translations (P) between stacking positions A, B, and C, lying in the close-packed planes, a translation ($\frac{1}{2}C$) of one close-packed layer spacing perpendicular to the close-packed planes, and a combination of these two displacements, $P+\frac{1}{2}C$ (after Drum). The displacement $P+\frac{1}{2}C$ corresponds to the translation between nitrogen atoms in adjacent close-packed planes.

Isolated faults of both types were imaged using several different diffracting conditions in order to determine their fault vectors, as shown in Fig. 8. The faults in the close-packed planes were visible for $g=0002$, $\bar{1}01\bar{1}$, $\bar{1}010$, $\bar{2}020$ and almost invisible for $g=11\bar{2}0$ and $g=\bar{3}030$. Using the criterion $g\cdot R=$ integer for visibility, a displacement vector of $\frac{1}{2}C$ ($R=1/2[0001]$) can be eliminated as the faults are visible for $g=\bar{1}010$ and $g=\bar{2}020$. Two types of faults consisting of P vectors alone can arise. The first is an extrinsic fault which is produced by a shear on two adjacent planes of total fault vector $-P+P$. As this is a lattice vector, such a fault should not be detectable by diffraction contrast and so can be eliminated. The second possible fault consisting of P vectors is an intrinsic fault produced by a single shear of P ($R=1/3[10\bar{1}0]$). The appearance of the faults for $g=\bar{1}010$, $g=\bar{2}020$ and the weak contrast for $g=\bar{3}030$ and disappearance for $g=11\bar{2}0$ suggest the presence of a P component to the fault vector. It is not possible, however, to distinguish among the three possible P vectors by fault contrast as they differ only by a lattice vector. It is also difficult to distinguish between faults of the type P and $P+\frac{1}{2}C$ as pointed out by Drum (*24*). However, as can be seen from Table I the phase factor introduced by faults of displacement vector P for $g=\bar{1}010$ and $\bar{1}01\bar{1}$ is $+2\pi/3$ in both cases. For faults of displacement vector $P+\frac{1}{2}C$, $\alpha=-1\pi/3$ for $g=\bar{1}01\bar{1}$ and $\alpha=+2\pi/3$ for $g=\bar{1}010$. The contrast of the outer fringe is dependent on α, i.e., dark for $\alpha=-1\pi/3$, $-2\pi/3$ and light for $\alpha=+1\pi/3$, $+2\pi/3$ (*25*). A change in contrast of the outer fringe in images from $g=\bar{1}010$ to

TABLE I

VALUES OF THE PHASE FACTOR $\alpha=2\pi\ g\cdot R$ FOR VARIOUS g AND R FOR FAULTS IN $BeSiN_2$ STRUCTURE

R / $2\pi g$	P / $\frac{1}{3}[10\bar{1}0]$	$\frac{1}{2}C$ / $\frac{1}{2}[0001]$	$P+\frac{1}{2}C$ / $\frac{1}{6}[20\bar{2}3]$	$P-\frac{1}{2}C$ / $\frac{1}{6}[\bar{2}02\bar{3}]$
$2\pi(0002)$	0	0	0	0
$2\pi(\bar{1}01\bar{1})$	$+2\pi/3$	π	$-1\pi/3$	$-1\pi/3$
$2\pi(\bar{1}010)$	$+2\pi/3$	0	$+2\pi/3$	$+2\pi/3$
$2\pi(\bar{2}020)$	$-2\pi/3$	0	$-2\pi/3$	$-2\pi/3$
$2\pi(\bar{3}030)$	0	0	0	0
$2\pi(11\bar{2}0)$	0	0	0	0

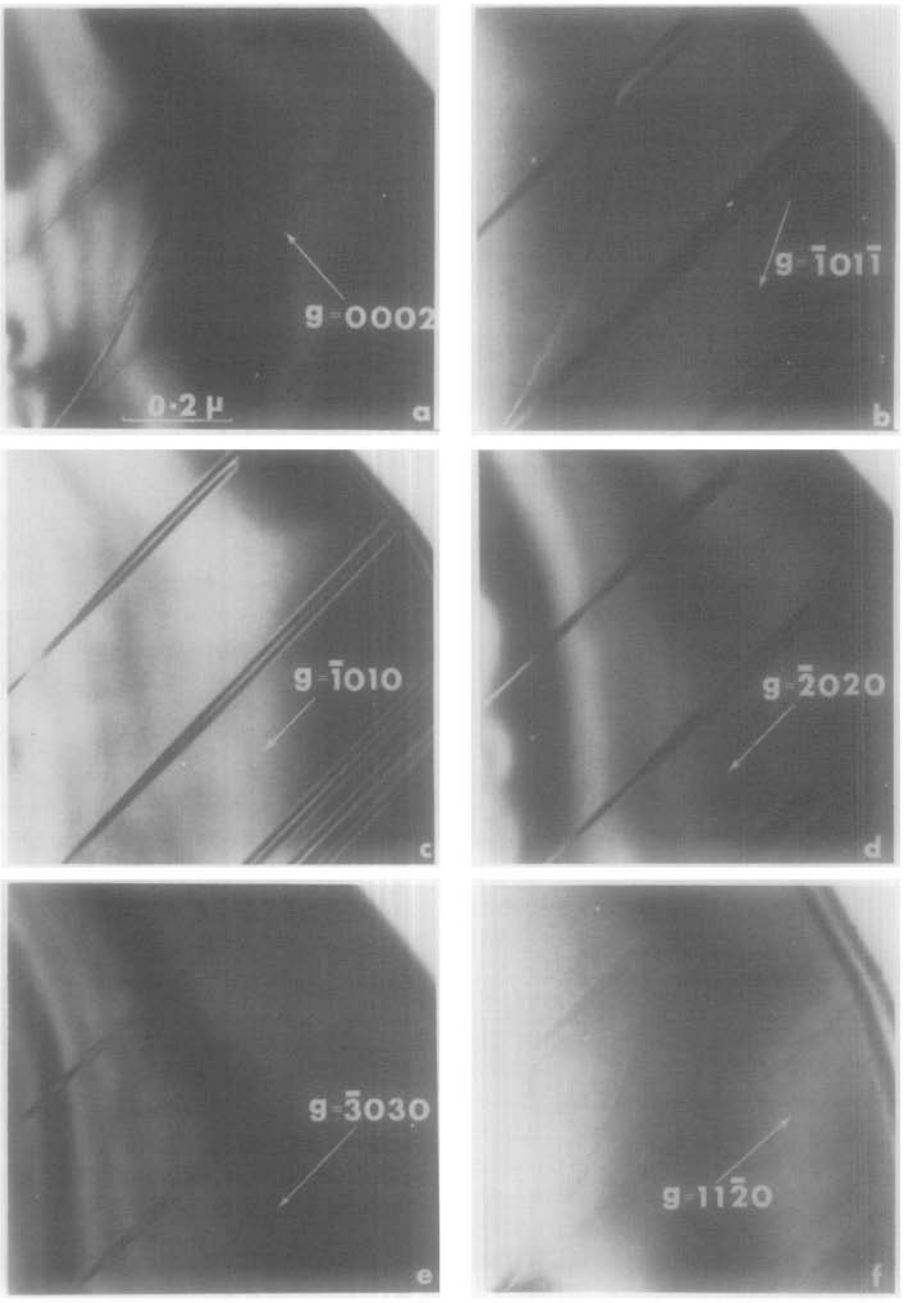

FIG. 8. Contrast from isolated faults in a $BeSiN_2$ grain for the diffracting conditions (a) $g = 0002$, (b) $g = \bar{1}01\bar{1}$, (c) $g = \bar{1}010$, (d) $g = \bar{2}020$, (e) $g = \bar{3}030$, and (f) $g = 11\bar{2}0$.

$g = \bar{1}01\bar{1}$ therefore occurs only if a component $\frac{1}{2}C$ is present in the fault vector. The appearance of a dark outer fringe for $g = \bar{1}01\bar{1}$ (Fig. 9b) and a light fringe for $g = \bar{1}010$ (Fig. 8c) indicates the presence of a component $\frac{1}{2}C$ in the fault vector. The probable displacement vector for the faults lying in the close-packed planes is thus of the type $P + \frac{1}{2}C$, i.e., for the faults shown in Fig. 8, $R = 1/6[20\bar{2}3]$.

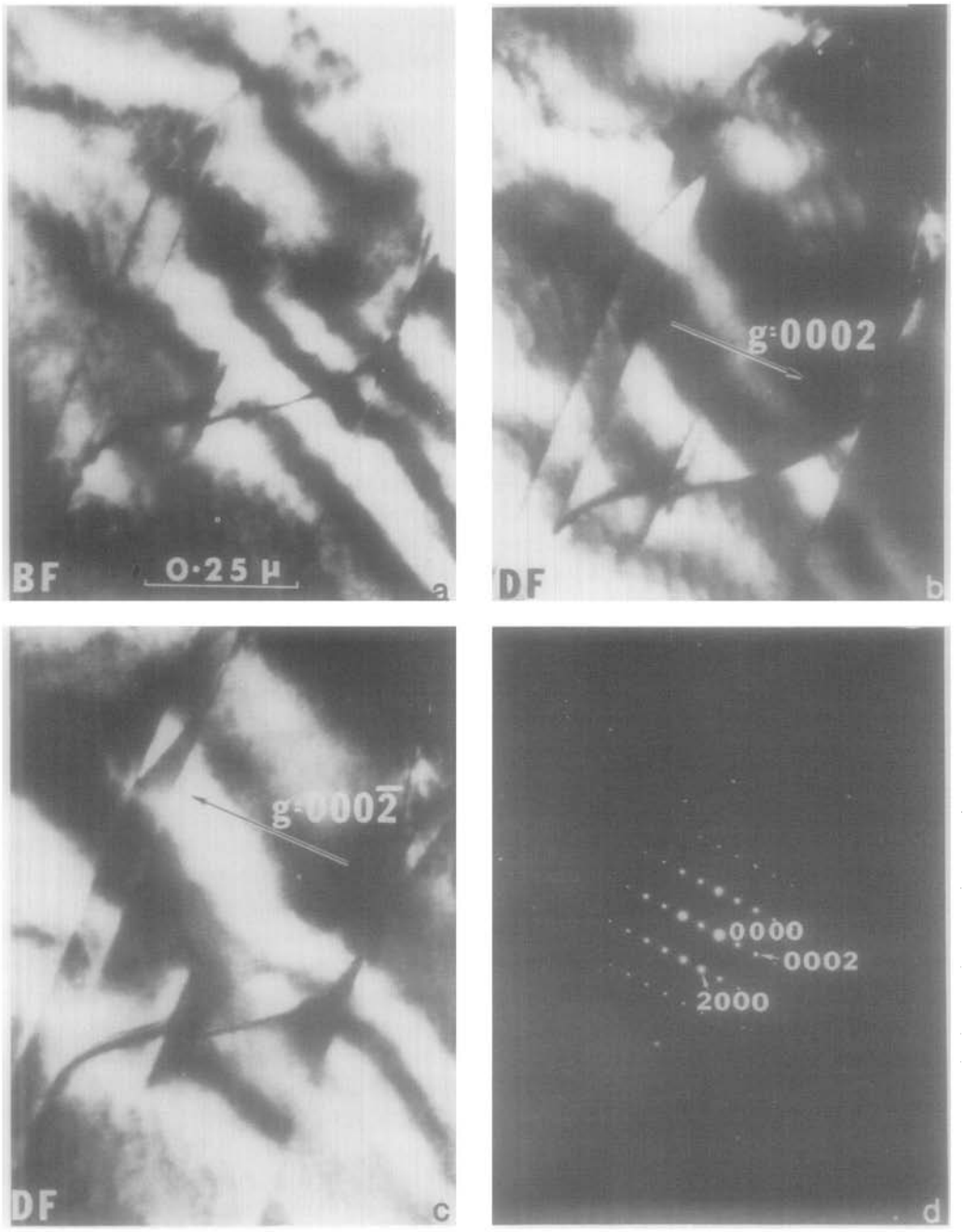

FIG. 9. Bright field and two dark fields of enantiomorphic domains in $BeSiN_2$. Differential contrast between domains arises in dark field (b) $g = 0002$ and (c) $g = 000\bar{2}$. The corresponding diffracting condition is shown in (d). Operating voltage is 650 kV.

The complete disappearance of faults for $g = \bar{3}030$ and $g = 0002$ should occur for $R = 1/6[20\bar{2}3]$, but this is not observed. The weak appearance of fault fringes for $g = \bar{3}030$ and complete disappearance for $g = 11\bar{2}0$ suggests that the displacement in $[10\bar{1}0]$ is not exactly $1/3[10\bar{1}0]$, but such that $g \cdot R = \text{integer} \pm 0.02$ for $g = 11\bar{2}0$ and

$g \cdot R \neq \text{integer} \pm 0.02$ for $g = \bar{3}030$ so that incomplete disappearance occurs for $g = \bar{3}030$. These results follow from the criterion that $g \cdot R = \text{integer} \pm 0.02$ for complete disappearance of faults as demonstrated by Hirsch *et al.* (*26*). The strong appearance of the faults for $g = 0002$ implies that the [0001] component of the displacement vector is not exactly $\frac{1}{2}C$ ($R = 1/2[001]$), but some nonintegral value. These results and the observation of strain contrast associated with some of the faults (bottom right of Fig. 8a) imply some distortion of the lattice and/or change in interatomic spacing is associated with the formation of the faults.

The curved faults were visible for $g = 0002$ and $g = \bar{1}01\bar{1}$ and invisible for $g = \bar{1}010$, $\bar{2}020$, $\bar{3}030$, and $11\bar{2}0$ (Fig. 8). These observations are not consistent with any simple displacement for the faults. However, the wurtzite structure is noncentrosymmetric and exists in two forms: one in which all upward pointing tetrahedral sites are occupied by atoms and the other in which all downward pointing sites are filled. A boundary between the two forms would be visible for all reflections from noncentrosymmetric planes, i.e., planes not perpendicular to the close-packed planes with indices h, k, i, l where $l \neq 0$. The boundary would be invisible for $g[u, v, t, 0]$. The faults lying in curved planes, therefore, exhibit contrast consistent for enantiomorphic boundaries in a wurtzite structure. This result was further substantiated by dark field imaging of faulted grains using $\pm g = 0002$ with several other beams simultaneously strongly excited. The violation of Friedel's law for these noncentrosymmetric reflections gives rise to different intensities from the two enantiomorphic forms (*27*) (Fig. 9). A thin area of the specimen was selected to reduce the effects of inelastic scattering, which reduces the difference in contrast between the two forms. The high-voltage microscope (650 kV) was used to reduce further the effects of inelastic scattering and to excite more reflections in the multibeam situation. Contrast from the two forms reversed on changing the sign of g and it can be seen that parts of the faults in the close-packed planes are also enantiomorphic boundaries (*28*).

The density of faults in the close-packed planes varied greatly from grain to grain. In Fig. 10 a series of images across a single grain of $BeSiN_2$ is shown. A very high density of faults is seen edge on, the density increasing from top to bottom, along the direction of the arrows. In the top image to the left, the grain is fault free. A selected area electron diffraction pattern from this region indicates it has a $BeSiN_2$ structure. A selected area diffraction (SAD) pattern taken with the intermediate aperture centered on the middle region contained a continuous streak in the [001]* direction. In an SAD pattern from the lower region, a continuous streak was again observed; only seven evenly spaced maxima in the streak occur from the transmitted beam up to and including the reflection from the close-packed planes. The maxima are suggestive of a preferential periodicity of seven close-packed plane spacings in the lattice of 16.4 Å.

By using the electron microscopy images in Fig. 10 as a diffraction grating for a laser light source the periodicity and spacing of the faults were examined (*29*). Using a small aperture (200 Å, effective diameter), isolated regions of regularly spaced faults were detected giving distinct reflections in optical diffraction patterns. The camera length of the optical bench was determined, using a standard grating in order to determine the spacing of faults from the spacing of reflections in the optical diffraction patterns. Using this technique three distinct regular fault periodicities were found, 21.1, 16.3, and 14.2 Å from regions 1, 2, and 3, respectively, in Fig. 10. These correspond to periodicities of nine, seven, and six close-packed layer spacings between faults.

Assuming each fault in a regular array has the experimentally determined displacement

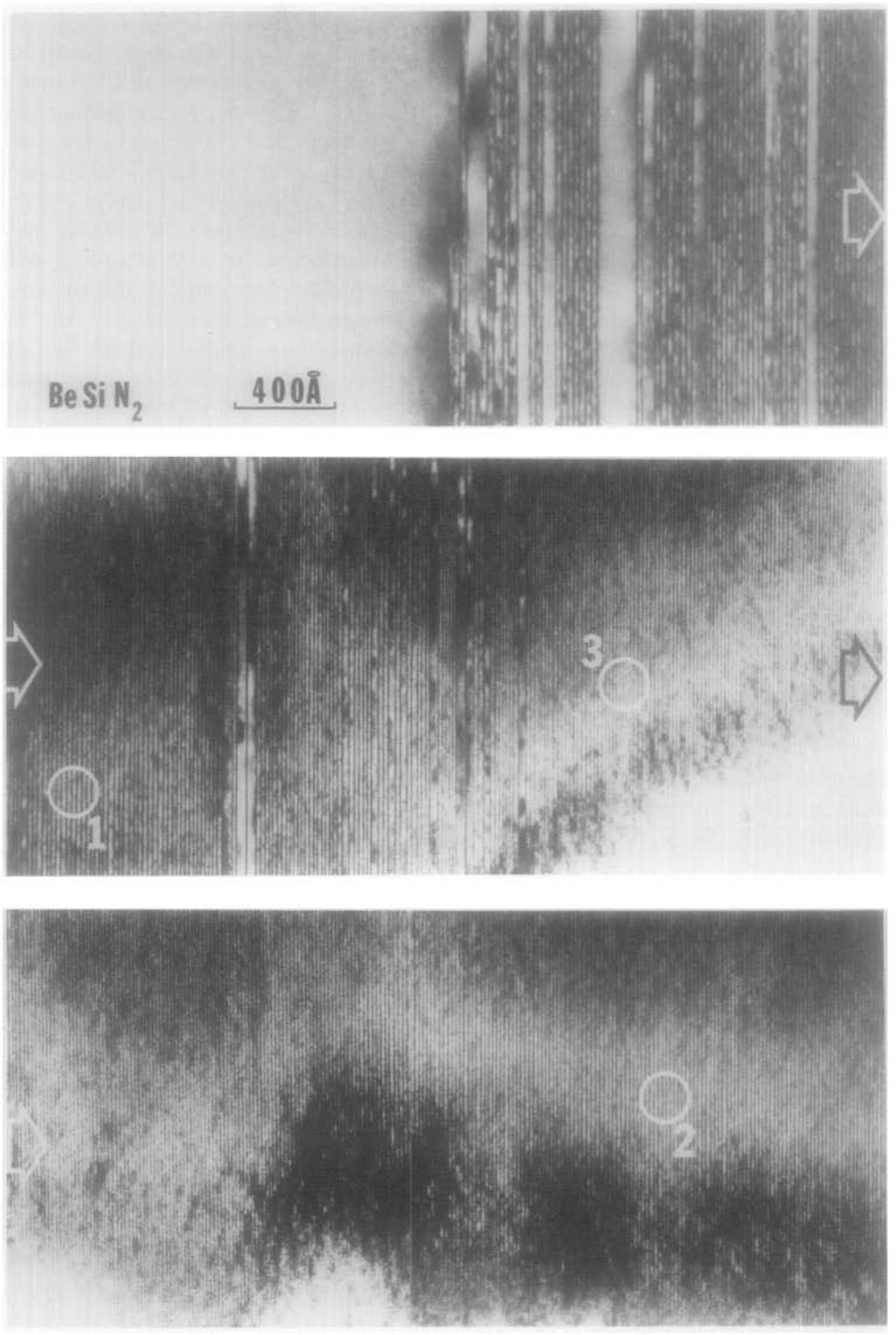

FIG. 10. A series of bright field images taken across a single grain of highly faulted $BeSiN_2$ structure.

vector of $\frac{1}{6}\langle 20\bar{2}3\rangle$, the structure of a regularly faulted region can be deduced. The effect of this displacement vector on a perfect wurtzite structure is to shear one layer of nitrogen atoms to the position of nitrogen atoms in the next close-packed plane (Figs. 11a and b). This effectively removes one layer of nitrogen atoms from the structure leaving an excess of metal atoms in a cubic stacked nitrogen lattice. The shear in creating a cubic layer forms non-base-sharing tetrahedral sites capable of accommodating the excess metal atoms. The composition of the layer is then M_2X and has the same structure as a single M_2X layer in a polytype structure. The structure produced by a regular array of faults is thus identical to that of a polytype structure. The regular periodicities of nine, seven, and six close-packed layers observed in Fig. 10 correspond, respectively, to thin domains $27R$, $21R$, and $12H$ structures.

IV. Discussion

IV.1. Stoichiometry and Polytype Structures

The observations made in the previous sections and their interpretation confirm the correctness of the $Be_xSi_yN_z$ polytype structures as determined by Thompson using X-ray analysis (*5*). These structures in which a regular arrangement of faults accommodates changes in composition are analogous to the so-called shear structures observed in complex metal oxides (*30–32*). In such oxides, two-dimensional arrays of "crystallographic shear faults" transform the basic oxide structure to a structure of different composition and unit-cell dimensions. The unit-cell dimensions depend on the spacing between shear faults, and as the spacing varies with composition, a complete homologous series of structures occurs as composition changes. The above results suggest that in the $BeSiN_2$–Be_3N_2 system, a one-dimensional array of crystallographic shear faults ($R = 1/6[20\bar{2}3]$) form in the ordered wurtzite $BeSiN_2$ structure as the composition changes. These faults produce a series of structures in which only one unit-cell dimension is changed with composition, i.e., the observed polytype series. The extra metal atom site per nitrogen atom in the fault makes them favorable sites for lower valency Be^{2+} atoms as this results in local charge compensation within the structure and so reduces the electrostatic imbalances between fault and matrix. Complete charge compensation can be produced if all metal atom sites in the M_2X layer and the net MX layer are occupied by beryllium atoms to form a block two close-packed layer thick of composition Be_3N_2. In this way an excess of beryllium atoms can be accommodated in the $BeSiN_2$ structure.

For small deviations from the exact $BeSiN_2$ composition toward a composition of Be_3N_2, isolated faults of this kind can accommodate the excess of beryllium atoms; their density increasing as larger deviations from stoichiometry occur. At some composition along the $BeSiN_2$–Be_3N_2 tie line the faults can no longer be considered as being isolated and start to interact with adjacent faults due to their high density and hence close proximity. Regular arrays of faults then

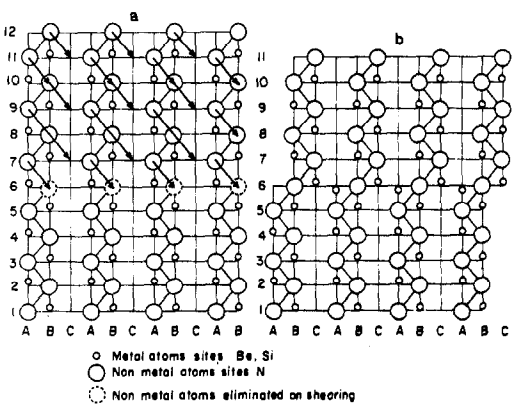

FIG. 11. Diagram of the stacking produced by a single fault in the close-packed plane of a wurtzite structure $R = 1/6(20\bar{2}3)$ (referred to wurtzite unit cell). $(01\bar{1}0)$ orientation planar section. (a) Unfaulted structure, (b) faulted structure.

arise so as to minimize their interaction energy, tending to form the polytype structures. The overall composition of a region of faulted structure is determined by the number of $BeSiN_2$ close-packed layers per fault. Clearly, perfectly regular faulting can only occur for integral values of this ratio and hence for specific compositions and metal to nonmetal atom ratios. At intermediate compositions, intermixed fault spacings will occur producing irregularly twinned structures, as observed in Section III.4.

The results of Section III.6 suggest that the first member of the polytype series is 27*R* as found by X-ray analysis (*5*). This corresponds to a fault spacing of nine close-packed layers, although interaction probably extends over larger distances as suggested by the common occurrence of fault pairs 30–40 Å apart. The anomalous absence of evidence for a 16*H* polytype in Section III.6 and X-ray diffraction patterns (*5*) remains to be explained. It is possible, though, that such a regular spacing of faults (eight close-packed layers) has an unfavorable interaction energy, preventing its formation. All other regular fault arrangements have been observed using X-ray techniques (*5*, *33*).

At compositions approaching Be_3N_2, $BeSiN_2$ layers can no longer separate all the faults. The structure produced by such an arrangement is that of β-Be_3N_2 consisting of two cubic stacked Be_3N_2 fault layers displaced with respect to each other to form a hexagonal unit cell.

Each Be_3N_2 fault layer resembles a block two close-packed layers thick of β-Be_3N_2 structure in a $BeSiN_2$ matrix. By a proportionate summing of the extreme members of the series in each polytype, a composition for each polytype can be predicted (Table II). The predicted compositions are found to match those found experimentally. Adopting a simplistic view of each polytype structure by considering them to be made up of noninteracting layers of β-Be_3N_2 and $BeSiN_2$

TABLE II

COMPOSITIONS AND *c*-SPACINGS OF POLYTYPES IN THE $BeSiN_2$–Be_3N_2 SERIES[a]

Polytype	$M:X$	No. layers Be_3N_2	No. layers $BeSiN_2$	Compositions		*c*-Spacings (Å)	
				Predicted	Experimental[b]	Predicted	Experimental[c]
4*H*/Be_3N_2	3:2	4	—	Be_3N_2	Be_3N2	9.693	9.693
9*R*	4:3	6	3	Be_7SiN_6	—	12.567	—
8*H*	5:4	4	4	Be_4SiN_4	Be_4SiN_4	19.064	19.22
15*R*	6:5	6	9	$Be_9Si_3N_{10}$	$Be_9Si_3N_{10}$	35.625	36.32
12*H*	7:6	4	8	$Be_5Si_2N_6$	$Be_5Si_2N_6$	28.44	29.10
21*R*	8:7	6	15	$Be_{11}Si_5N_{14}$	$Be_{11}Si_5N_{14}$	49.68	50.98
16*H*?	9:8	4	12	$Be_6Si_3N_8$	—	37.81	—
27*R*?	10:9	6	21	$Be_{13}Si_7N_{1E}$	$Be_{13}Si_7N_{18}$	63.74	65.11
$BeSiN_2$	1:1	—	2	$BeSiN_2$	$BeSiN_2$	4.69	4.69

[a] β-Be_3N_2: hexagonal $a_0 \doteq 2.842$ Å, $c_0 = 9.706$ Å, close-packed layer spacing 2.423 Å. $BeSiN_2$: orthorhombic, ordered wurtzite structure, $a_0 = 4.977$ Å, $b_0 = 5.747$ Å, $c_0 = 4.674$ Å, close-packed layer spacing = 2.343 Å. For convenience, a unit cell with the same base vectors as those for $BeSiN_2$ was chosen to describe the polytype structures, viz., $a_0 \simeq 4.9$ Å, $b_0 \simeq 5.7$ Å, and c_0 a variable multiple of close-packed layer spacing. This enables all the polytype structures to be described using the same base vectors for the unit cell. The unit cell described in this way does not reflect the full symmetry of each polytype, which may be rhombohedral or hexagonal, depending on the stacking of the planes.

[b] From Huseby *et al.* (*6*).

[c] From Thompson (*5*).

structures, stacked in the appropriate manner, a prediction of the unit-cell dimensions in the [001] direction can be made (Table II). Superficially the agreement with experiment seems good but it is found that the linear variation with composition predicted is not obeyed. A more realistic view in which interatomic forces and matching of atomic positions across the block interfaces are considered may account for this. Indeed some evidence was found for elastic distortion of the matrix being associated with isolated faults and fault pairs and also a change in close-packed layer spacing being associated with fault formation (Section III.6). It is conceivable also that such an elastic distortion could play an important role in fault interactions and so polytype formation.

IV.2. Polytypes in Other Sialon Systems

Similar polytype series to those in the $BeSiN_2$–Be_3N_2 system have been reported in other sialon systems (*4*). In the Be–Si–O–N system an almost identical series of polytypes occurs for compositions BeO–Be_3N_2. Both nitrogen and oxygen atoms form the close-packed lattice, and beryllium atoms occupy tetrahedral cation sites. X-Ray analysis has identified the arrangement of nonmetal and metal atoms as being the same as those in the $BeSiN_2$–Be_3N_2 series. The series may be described as in the $BeSiN_2$–Be_3N_2 system as the faulting of a wurtzite structure (BeO) to accommodate changes in composition along the BeO–Be_3N_2 tie line. Description of the polytypes as intergrowths of blocks of BeO and Be_3N_2 structure in a manner analogous to that of the $BeSiN_2$–Be_3N_2 series allows the composition of each polytype to be correctly predicted (Table III). A prediction of unit-cell dimensions, again assuming no interaction between structural blocks, shows better agreement with experiment than found in the $BeSiN_2$–Be_3N_2 system (Table III), a linear variation in the *c* unit-cell dimension occurring with composition.

Identical polytype phases in the two systems were found to extend along the same lines of constant metal to nonmetal atom ratio in the Be–Si–O–N system (Fig. 1). Continuous solid solutions between each polytype, however, were not found. It is possible that polytype structures consisting of more complex structural intergrowths occur in this region of the phase diagram.

TABLE III

COMPOSITIONS AND *c*-SPACINGS OF POLYTYPES IN THE BeO–Be_3N_2 SERIES[a]

Polytype	*M*:*X*	No. layers Be_3N_2	No. layers Be_2O_2	Compositions		*c*-Spacings Å	
				Predicted	Experimental[b]	Predicted	Experimental[c]
4*H*/Be_3N_2	3:2	4	—	Be_3N_2	Be_3N_2	9.693	9.693
9*R*	4:3	6	3	Be_4ON_2	—	21.099	—
8*H*	5:4	4	4	$Be_4O_2N_2$	—	18.44	—
15*R*	6:5	6	9	$Be_6O_3N_2$	$Be_6O_3N_2$	34.22	34.58
12*H*	7:6	4	8	$Be_7O_4N_2$	—	17.19	—
21*R*	8:7	6	15	$Be_8O_5N_2$	$Be_8O_5N_2$	47.34	47.87
16*H*?	9:8	4	12	$Be_9O_6N_2$	—	35.94	—
27*R*?	10:9	6	21	$Be_{10}O_7N_2$	—	60.47	61.05
BeO	1:1	—	2	BeO	BeO	4.38	4.38

[a] Close-packed layer spacing of β-Be_3N_2 = 2.423 Å; close-packed layer spacing of BeO = 2.187 Å.
[b] From Huseby *et al.* (*6*).
[c] From Thompson (*5*).

High-resolution electron microscopy of samples of these materials should help establish this point.

Extensive polytypism similar to that in the Be–Si–O–N system also occurs in the Si–Al–O–N system at AlN-rich compositions, only with the role of metal and nonmetal atoms reversed. Again, their description as faulted versions of the wurtzite structure (AlN) is possible, wherein extra nonmetal atoms are accommodated at sites with favorable coordination created by the faults.

Conclusions

The main results of this investigation can be summarized as follows:

(1) The stacking sequence of close-packed planes of atoms in the $BeSiN_2$–Be_3N_2 polytype structures derived from X-ray data is confirmed by real space high-resolution electron microscopy studies.

(2) The polytypes may be described in terms of regular faulting of the ordered wurtzite $BeSiN_2$ structure. Each fault (displacement vector $1/6\langle 20\bar{2}3\rangle$) creates a layer of cubic stacked nitrogen atoms in which tetrahedral metal atom sites no longer share bases. Ths allows an excess of beryllium atoms to be accommodated in the structure. For a small excess isolated faults occur, their density increasing as the beryllium content increases. At high densities the faults interact and so form regular arrays for specific compositions.

(3) Each fault may be considered as a coherent layered intergrowth of β-Be_3N_2 in a $BeSiN_2$ matrix. This model allows the correct composition of each polytype as well as other prominent crystallographic features to be directly predicted.

Acknowledgments

We are grateful to Dr. L. J. Gauckler, Max-Planck-Institut fur Metallforschung, Stuttgart, for providing the samples. We also thank Professor K. H. Jack of Newcastle University and D. R. Clarke of the Science Center, Rockwell International, for their collaboration in this work. Financial support is provided by the National Science Foundation.

We gratefully acknowledge the assistance of the support staff and facilities of the Lawrence Berkeley Laboratory.

References

1. K. H. JACK AND W. I. WILSON, *Nature Phys. Sci.* **23E**, 28 (1972).
2. Y. OYAMA AND O. KAMIGAITO, *Japan J. Appl. Phys.* **10**, 1637 (1972).
3. A. TSUGE, H. INOUE, AND K. KOMEYA, *in* "Tenth Symposium on Basic Ceramics," Osaka (1972).
4. K. H. JACK, *J. Mater. Sci.* **11**, 1135 (1Z76).
5. D. P. THOMPSON, *J. Mater. Sci.* **11**, 1377 (1976).
6. I. C. HUSEBY, H. L. LUKAS, AND G. PETZOW, *J. Amer. Ceram. Soc.* **58**, 377 (1975).
7. L. J. GAUCKLER, H. L. LUKAS, AND G. PETZOW, *J. Amer. Ceram. Soc.*, **58**, 346 (1975).
8. R. J. LUMBY, B. NORTH, AND A. J. TAYLOR, *in* "Special Ceramics 6" (P. POPPER, Ed.), p. 283, The British Ceramic Research Association, Stoke-on-Trent (1975).
9. R. R. WILLS, R. W. STEWART, AND J. M. WIMMER, *Amer. Ceram. Soc. Bull.* **55**, 975 (1976).
10. C. A. ANDERSSON, F. F. LANGE, AND J. L. ISKOE, "Westinghouse Electric Corp. Tech. Report," Vol. 3 (October 15, 1975).
11. G. R. TERWILLINGER AND F. F. LANGE, *J. Mater. Sci.* **10**, 1169 (1975).
12. R. R. WILLS, R. W. STEWART, J. A. CUNNINGHAM, AND J. M. WIMMER, *J. Mater. Sci.* **11**, 749 (1976).
13. P. DREW AND M. H. LEWIS, *J. Mater. Sci.* **9**, 1833 (1974).
14. L. S. RAMSDELL, *Amer. Mineral.* **32**, 64 (1947).
15. R. PAULUS, *Z. Phys. Chem. Abt. B* **22**, 305 (1933).
16. P. ECKERLIN AND A. RABENAU, *Z. Anorg. Allg. Chem.* **304**, 218 (1960).
17. D. HALL, G. E. GURR, AND G. A. JEFFREY, *Z. Anorg. Allg. Chem.* **369**, 108 (1969).
18. P. ECKERLIN, *Z. Anorg. Allg. Chem.* **353**, 225 (1967).
19. W. L. BELL, *J. Appl. Phys.* **47**, 1676 (1976).
20. D. R. CLARKE, T. M. SHAW, AND D. P. THOMPSON, *J. Mater. Sci.* **13**, 217 (1978).
21. T. M. SHAW AND G. THOMAS, *Science* **202**, 625 (1978).
22. S. IIJIMA AND P. R. BUSECK, *in* "Electron Microscopy in Mineralogy" (H. R. WENK, Ed.), p. 319, Springer-Verlag (1976).

23. S. ANDERSSON AND B. G. HYDE, *J. Soid State Chem.* **9**, 92 (1974).
24. C. M. DRUM, *Phil. Mag.* **11**, 313 (1965).
25. R. GEVERS, A. ART, AND S. AMELINCKX, *Phys. Status Solidi* **3**, 1563 (1963).
26. P. B. HIRSCH *et al.*, "Electron Microscopy of Thin Crystals," p. 165, Butterworths, London (1965).
27. R. SERNEELS, M. SNYKERS, P. DELAVIGNETTE, R. GEVERS, AND S. AMELINCKX, *Phys. Status Solidi B* **58**, 277 (1973).
28. O. VAN DER BIEST AND G. THOMAS, *Acta Crystallogr. Sect. A* **31**, 70 (1975).
29. R. SINCLAIR, R. GRONSKY, AND G. THOMAS, *Acta Met.* **24**, 789 (1976).
30. S. IIJIMA AND J. G. ALLPRESS, *J. Solid State Chem.* **7**, 94 (1973).
31. J. V. LANDUYT, *J. Phys. (Paris)* **35**, C7–53 (1974).
32. S. IIJIMA, *Acta Crystallogr. Sect. A* **31**, 7E4 (1975).
33. D. P. THOMPSON AND L. J. GAUCKLER, *J. Amer. Ceram. Soc.* **60**, 9–10, 470m (1977).